



Article

Modified MHD Radiative Mixed Convective Nanofluid Flow Model with Consideration of the Impact of Freezing Temperature and Molecular Diameter

Umar Khan ¹, Adnan Abbasi ², Naveed Ahmed ³ , Sayer Obaid Alharbi ⁴, Saima Noor ⁵, Ilyas Khan ^{6,*}, Syed Tauseef Mohyud-Din ³ and Waqar A. Khan ⁷ 

¹ Department of Mathematics and Statistics, Hazara University, Mansehra 21120, Pakistan; umar_jadoon4@yahoo.com

² Department of Mathematics, Mohi-ud-Din Islamic University Nerian Sharif, Azad Jammu & Kashmir 12080, Pakistan; adnan_abbasi89@yahoo.com

³ Department of Mathematics, Faculty of Sciences, HITEC University Taxila Cantt, Punjab 47080, Pakistan; nidojan@gmail.com (N.A.); syedtauseefs@hotmail.com (S.T.M.-D.)

⁴ Department of Mathematics, College of Science Al-Zulfi, Majmaah University, Al-Majmaah 11952, Saudi Arabia; so.alharbi@mu.edu.sa

⁵ Department of Mathematics, COMSATS University Islamabad, Abbottabad 22010, Pakistan; saimanoor@ciit.net.pk

⁶ Faculty of Mathematics and Statistics, Ton Duc Thang University, Ho Chi Minh City 72915, Vietnam

⁷ Department of Mechanical Engineering, College of Engineering, Prince Mohammad Bin Fahd University, Al Khobar 31952, Saudi Arabia; wkhan1956@gmail.com

* Correspondence: ilyaskhan@tdtu.edu.vn

Received: 13 March 2019; Accepted: 16 April 2019; Published: 25 June 2019



Abstract: Magnetohydrodynamics (MHD) deals with the analysis of electrically conducting fluids. The study of nanofluids by considering the influence of MHD phenomena is a topic of great interest from an industrial and technological point of view. Thus, the modified MHD mixed convective, nonlinear, radiative and dissipative problem was modelled over an arc-shaped geometry for $\text{Al}_2\text{O}_3 + \text{H}_2\text{O}$ nanofluid at 310 K and the freezing temperature of 273.15 K. Firstly, the model was reduced into a coupled set of ordinary differential equations using similarity transformations. The impact of the freezing temperature and the molecular diameter were incorporated in the energy equation. Then, the Runge–Kutta scheme, along with the shooting technique, was adopted for the mathematical computations and code was written in Mathematica 10.0. Further, a comprehensive discussion of the flow characteristics is provided. The results for the dynamic viscosity, heat capacity and effective density of the nanoparticles were examined for various nanoparticle diameters and volume fractions.

Keywords: arched surface; nonlinear thermal radiation; molecular diameter; Al_2O_3 nanoparticles; streamlines; isotherms; RK scheme

1. Introduction

The liquids regularly used in heat transfer applications, such as water, propylene glycol, ethylene glycol, kerosene oil, engine oil and transformer oil, are extensively used in industry and in thermal power plants. Due to their reduced thermal conductivity, these liquids do not have effective heat transfer characteristics. However, for a great deal of industrial production, remarkable amounts of heat are required. The thermal conductivity of the solid materials, such as different metals and oxides, is very high in comparison with regular liquids. Thus, scientists and engineers hypothesized that the heat

transfer in working fluids could be enhanced by mixing in the nanoparticles in above regular liquids. Finally, Choi [1] developed a colloidal composition that has effective heat transfer characteristics, as compared to regular fluids. Choi [1] unlocked a new innovative research area and researchers, scientists and engineers focused on the analysis of nanofluids. Before the development of nanofluids, heat transfer was a major problem from an industrial point of view, since considerable amounts of heat transfer were required for a great deal of technological and industrial production, and regular liquids failed to provide the desired amount of heat. Thermal conductivity plays a major role in the heat transfer rate of nanofluids. Thus, several theoretical models were proposed for thermal conductivity. The thermal conductivity model was developed by Maxwell in 1873 [2], who considered nanosized particles, and this can be considered the origin of the concept of the nanofluids.

Several theoretical models based on nanoparticle characteristics that take into account the effects of temperature and the shape and diameter of nanoparticles, as well as Brownian motion, have been presented. In 1935, Bruggemann [3] constructed a thermal conductivity correlation for spherical nanoparticles that was limited to high concentration patterns. The behavior of thermal conductivity was developed by Hamilton [4] in 1962, who explored the effects of nanoparticle shape. In 1996, Lu and Lin [5] proposed a model incorporating the effects of Brownian dynamics. The thermal conductivity model for the interaction between the nanoparticles and their surrounding liquid was developed by Koo and Kleinstreuer [6,7]. Xue [8] developed a thermal conductivity model for carbon nanotubes. In 2005, Prasher et al. [9] found a correlation by considering the influence of convection on the thermal conductivity of nanoparticles. In 2006, Li [10] made apparent the influence of temperature on thermal conductivity and outlined a correlation for $\text{Al}_2\text{O}_3/\text{H}_2\text{O}$ and $\text{CuO}/\text{H}_2\text{O}$ nanofluids. In 2011, Corcione [11] developed a model for $\text{Al}_2\text{O}_3 + \text{H}_2\text{O}$ nanofluids by incorporating the effects of freezing temperatures. By incorporating thermal conductivity models, the above researchers presented various models and described the heat transfer enhancement due to thermal conductivity. Some useful studies for nanofluids are described in [12–16].

Similar to nanoparticles, carbon nanotubes also have high thermal conductivity and unique mechanical and chemical properties. Carbon nanotubes are subcategorized as either single or multiple walled carbon nanotubes. The concept of colloidal suspension in relation to carbon nanotubes was presented by Iijima [17]. After the development of the thermal conductivity correlation for carbon nanotubes, many studies were presented outlining thermal enhancement due to suspended carbon nanotubes. Recently, Ahmed et al. [18] explored the influence of thermal radiation and viscous dissipation on the flow of water suspended by carbon nanotubes. The effect of thermophysical characteristics of the nanotubes on the heat transfer enhancement water over a curved surface and non-parallel walls was described in [19,20], respectively.

Recently, the flow over an arc-shaped geometry has become a point of interest. Reddy et al. [21] recently modified the curve-shaped flow model for nonlinear radiative heat flux. They also examined the impact of the cross-diffusion phenomenon on heat and mass transfer. Another useful mechanism to enhance the fluid temperature is ohmic heating, which produces extra heat in the conductor, with electrons supplying energy to the atoms of the conductor through collisions. In 2017, Hayat et al. [22] examined the effects of resistive heating on the curve surface flow.

A literature review revealed that there have not yet been any studies of the impact of freezing temperatures and the diameter of nanoparticles on the flow of incompressible fluids due to the effects of nonlinear radiative heat flux, viscous dissipation, mixed convection and Lorentz forces. This study is presented to cover this significant gap. The nanofluids $\text{Al}_2\text{O}_3 + \text{H}_2\text{O}$ were used to study the characteristics of the flow and other effective thermophysical properties, such as effective density, heat capacity and thermal conductivity. The results for shear stress and local heat transfer are also described and discussed comprehensively. Finally, major findings of the study is presented.

2. Model Formulation

We considered the laminar time independent and the incompressible flow of the $\text{Al}_2\text{O}_3 + \text{H}_2\text{O}$ nanofluid by taking into account the influence of a nonlinear, radiative heat flux and the imposed variable magnetic field over an arc geometry situated in the curvilinear frame r and s . Further, the r -axis was perpendicular, and the arc was placed in the direction of s . The velocity and magnetic field were functions of s and mathematically described as below:

$$u_w(s) = \frac{b}{s^{-m}}, \hat{B}(s) = \frac{B_0}{(s^{0.5(m-1)})^{-1}},$$

It was assumed that the induced magnetic field was inconsequential, and therefore was not taken into consideration. The temperatures at the arched and the free surface were \hat{T}_w and \hat{T}_∞ , respectively. The value of $m > 1$ represented the flow over an arc shaped, which was nonlinearly stretched. $m = 1$ was for the flow of a linearly stretching geometry. Figure 1 presents the flow description in a curvilinear frame. The flow chart of the study presented in Figure 2.

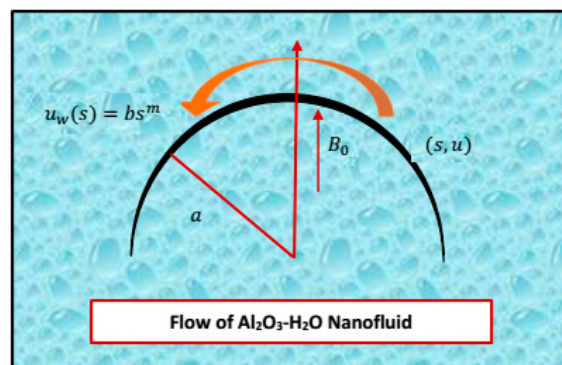


Figure 1. Flow description in a curvilinear frame.

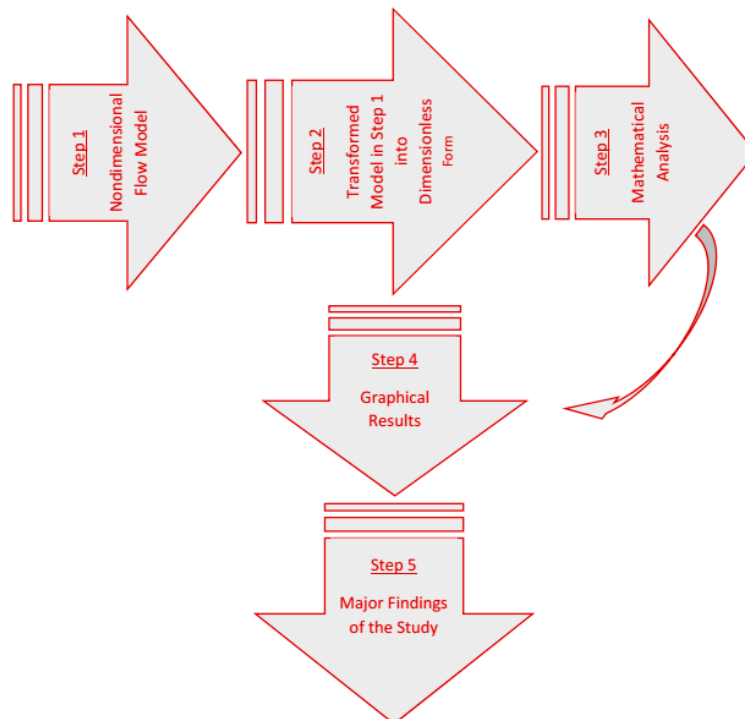


Figure 2. Flowchart of the study.

The $\text{Al}_2\text{O}_3 + \text{H}_2\text{O}$ nanofluid flow, incorporating the phenomena of Lorentz forces, viscous dissipation and nonlinear radiative heat flux, is described by the following system [21]:

$$\frac{\partial}{\partial r}(\hat{v}(r+a)) = 0, \quad (1)$$

$$\hat{u}^2 = \frac{\partial p}{\partial r}(r+a)(\rho_{nf})^{-1}, \quad (2)$$

$$\rho_{nf} \left(\hat{v} \frac{\partial \hat{u}}{\partial r} + \left(\frac{a}{r+a} \right) \hat{u} \frac{\partial \hat{u}}{\partial s} + \hat{u} \frac{\partial \hat{v}}{\partial r} \right) = - \frac{a}{(r+a)} \frac{\partial p}{\partial s} + \mu_{nf} \left(\frac{\partial^2 \hat{u}}{\partial r^2} + \left(\frac{1}{r+a} \right) \frac{\partial \hat{u}}{\partial r} - \left(\frac{1}{r+a} \right)^2 \hat{u} \right) - \sigma_{nf} B_0^2 \hat{u} + g(\rho\beta)_{nf}(T - T_\infty), \quad (3)$$

$$\frac{a}{(r+a)} \hat{u} \frac{\partial \hat{T}}{\partial s} + \hat{v} \frac{\partial \hat{T}}{\partial r} = \frac{k_{nf}}{(\rho C_p)_{nf}} \left(\frac{1}{(r+a)} \frac{\partial \hat{T}}{\partial r} + \frac{\partial^2 \hat{T}}{\partial r^2} \right) + \frac{\mu_{nf}}{(\rho C_p)_{nf}} \left(\frac{\partial \hat{u}}{\partial r} - \frac{\hat{u}}{(r+a)} \right)^2 - \frac{1}{(\rho C_p)_{nf}(r+a)} \frac{\partial}{\partial r}(q_R(r+a)), \quad (4)$$

with boundary conditions at the curve and far from the curve of:

At $r = 0$:

$$\left. \begin{aligned} \hat{u} &= bs^m \\ \hat{v} &= 0 \\ \hat{T} &= T_w \end{aligned} \right\}. \quad (5)$$

At $r \rightarrow \infty$:

$$\left. \begin{aligned} \hat{u} &\rightarrow 0 \\ \frac{\partial \hat{u}}{\partial r} &\rightarrow 0 \\ \hat{T} &\rightarrow T_\infty \end{aligned} \right\}. \quad (6)$$

The expression for nonlinear radiative heat flux is described as:

$$q_R = -4 \frac{\hat{\sigma}}{3} \hat{k} \frac{\partial}{\partial r}(\hat{T}^4) = -\frac{16}{3} \frac{\hat{\sigma}}{\hat{k}} \hat{T}^3 \frac{\partial \hat{T}}{\partial r}, \quad (7)$$

Equations (1)–(4) are the conservation of mass, momentum and energy, respectively. Further, the Stefan–Boltzmann law and adsorption coefficient are $\hat{\sigma}$ and \hat{k} , respectively. To enhance the thermal and physical characteristics of the model, the following effective models for thermophysical characteristics were used [23]:

$$\rho_{nf} = \left[(1 - \phi) + \frac{\phi \rho_p}{\rho_f} \right] \rho_f, \quad (8)$$

$$(\rho C_p)_{nf} = \left[(1 - \phi) + \frac{\phi (\rho C_p)_p}{(\rho C_p)_f} \right] (\rho C_p)_f, \quad (9)$$

$$\mu_{nf} = \mu_f \left(1 - 34.87 \left(\frac{d_{particle}}{d_{fluid}} \right)^{-0.3} \phi^{1.03} \right)^{-1}. \quad (10)$$

$$k_{nf} = k_f \left(1 + 4.4 \text{Re}_b^{0.4} \text{Pr} \left(\frac{T}{T_{freezing}} \right)^{10} \left(\frac{k_p}{k_f} \right)^{0.03} \phi^{0.66} \right), \quad (11)$$

$$(\rho\beta)_{nf} = \left[(1 - \phi) + \frac{\phi (\rho\beta)_p}{(\rho\beta)_f} \right] (\rho\beta)_f, \quad (12)$$

$$\sigma_{nf} = \sigma_f \left[1 + \frac{3(\Theta - 1)\phi}{(\Theta + 2) - (\Theta - 1)\phi} \right], \text{ where } \Theta = \frac{\sigma_p}{\sigma_f}. \quad (13)$$

In Equation (11), Re_b shows the Reynolds number due to Brownian motion, and is described in the following pattern:

$$Re_b(\mu_f) = d_p \rho_f u_b, \tag{14}$$

In Equation (14), the velocity of Brownian motion is calculated by the formula:

$$u_b = 2Tk_b(\pi d_p^2 \mu_f), \tag{15}$$

Here, k_b is the Stefan–Boltzmann coefficient and its value is 1.380648×10^{-23} (JK⁻¹). d_p represents the molecular diameter which is calculated by the expression [24]:

$$d_f = 6M^*(N^* \rho_f \pi)^{-1}, \tag{16}$$

The molecular weight of the regular liquid and Avogadro number are denoted by M^* and N^* , respectively. Further, the value of d_f is calculated as:

$$d_f = \left(\frac{6 \times 0.01801528}{998.62 \times (6.022 \times 10^{23}) \times \pi} \right)^{\frac{1}{3}} = 3.85 \times 10^{-10} \text{ nm}, \tag{17}$$

Table 1 shows the data for thermal conductivity, effective density, thermal expansion coefficient, and effective dynamic viscosity [23]:

Table 1. Thermal and physical characteristics of the fluid phase and nanoparticles at $T = 310$ K [23].

Properties	d_p (nm)	ρ (kg/m ³)	β (1/k)	c_p (J/Kg K)	μ_f (kg/ms)	k (W/mk)	σ (S/m)
H ₂ O	0.385	993	36.2×10^5	4178	695×10^6	0.628	0.005
Al ₂ O ₃	33	3970	0.85×10^5	765	-	40	0.05×10^6

The similarity transformations are described in the following set of equations [21]:

$$\left. \begin{aligned} \eta &= \sqrt{\frac{b}{v_{bf}}} s^{0.5(m-1)} r \\ \hat{u} &= bs^m L' \\ p &= \rho_{bf} b^2 s^{2m} P' \\ \hat{v} &= -\frac{a}{(r+a)} \sqrt{bv_{bf}} s^{0.5(m-1)} \{0.5(m+1)L + 0.5(m-1)\eta L'\} \\ N &= \frac{T-T_\infty}{T_w-T_\infty} \end{aligned} \right\} \tag{18}$$

To analyze the phenomena of nonlinear radiative heat flux, the following expression was used:

$$\hat{T} = T_\infty(1 + (\beta_w - 1)N) \tag{19}$$

The ratio of wall and free surface temperature was denoted by β_w .

The following model was attained after incorporating the similarity transformations and partial derivatives in Equations (1)–(4):

$$\begin{aligned} &\frac{1}{\left(1 - 34.87 \left(\frac{d_p}{d_f}\right)^{-0.3} \phi^{1.03}\right)} \left[(\eta + K)^3 L'''' + 2(\eta + K)^2 L''' - (\eta + K)L'' + L' \right] - \\ &\left[1 + \frac{3(\Theta-1)\phi}{(\Theta+2)-(\Theta-1)\phi} \right] M \left[(\eta + K)^3 L'' + (\eta + K)^2 L' \right] + \left((1 - \phi) + \frac{\phi(\rho\beta)_p}{(\rho\beta)_f} \right) \\ &\alpha \left((\eta + K)^3 N' + (\eta + K)^2 L \right) + \\ &\left\{ (1 - \phi) + \frac{\phi\rho_p}{\rho_f} \right\} K \left[\begin{aligned} &0.5(1 - 3m)(\eta + K)(L')^2 + 0.5(m + 1)(\eta + K)LL'' \\ &-0.5(m + 1)LL' + 0.5(m + 1)(\eta + K)^2 LL''' + \\ &(\eta + K)^2 0.5(1 - 3m)L'L'' \end{aligned} \right] = 0, \tag{20} \end{aligned}$$

$$\begin{aligned}
 Rd & \left[3(N')^3(1 + (\beta_w - 1)N)^2(\beta_w - 1)(\eta + K) + (1 + (\beta_w - 1)N)^3((\eta + K)N'' + N') \right] + \\
 & \left[1 + 4.4Re_b^{0.4} Pr \left(\frac{T}{T_{freezing}} \right)^{10} \left(\frac{k_p}{k_f} \right)^{0.03} \phi^{0.66} \right] ((\eta + K)N'' + N') + \\
 & \frac{PrEc}{\left(1 - 34.87 \left(\frac{d_p}{d_f} \right)^{-0.3} \phi^{1.03} \right) (\eta + K)} ((\eta + K)L'' - L')^2 = 0.
 \end{aligned}
 \tag{21}$$

In Equations (20) and (21), L and N are the functions of η . After solving, L and N provide the velocity and temperature distributions, respectively.

$$L(\eta) = 0, \quad L'(\eta) = 1, \quad N(\eta) = 1, \tag{22}$$

At $\eta \rightarrow \infty$:

$$L'(\eta) \rightarrow 0, \quad L''(\eta) \rightarrow 0, \quad N(\eta) \rightarrow 0, \tag{23}$$

Dimensionless quantities were described by the following formulas:

$$\begin{aligned}
 K &= a \sqrt{\frac{b}{v_{bf}}}, \quad Ec = \frac{b^2 s^{2m}}{(C_p)_f (T_w - T_\infty)}, \quad Rd = 16\hat{\sigma} \frac{T_\infty^3}{3kk_f}, \quad M = \frac{\sigma_f B_0^2}{\rho_f b}, \quad Pr = \frac{(c_p)_f \mu_f}{k_f}, \\
 \alpha &= Gr_s (Re_s^2)^{-1}, \quad Re_s = bs^2 (v_f)^{-1}, \quad Gr_s = s^3 (T_w - T_\infty) g \beta (v_f)^{-2}.
 \end{aligned}
 \tag{24}$$

Moreover, the dimensional formula for skin friction and local Nusselt number were defined as:

$$C_f = \tau_{rs} (\rho_f \hat{u}_w^2)^{-1}, \quad Nu_s = sq_w (k_f (T_w - T_\infty))^{-1}, \tag{25}$$

where,

$$\tau_{rs} = \left(\frac{\partial \hat{u}}{\partial r} - \frac{\hat{u}}{(a+r)} \right) \downarrow r=0, \quad q_w = -k_{nf} \frac{\partial \hat{T}}{\partial r} \downarrow r=0, \tag{26}$$

Drawing the values from Equation (26) into Equation (25), the following dimensionless formulas were obtained:

$$C_f (Re_s)^{\frac{1}{2}} = \frac{1}{\left(1 - 34.87 \left(\frac{d_p}{d_f} \right)^{-0.3} \phi^{1.03} \right)} (L''(0) - L'(0)K^{-1}), \tag{27}$$

$$Nu_s (Re_s)^{-\frac{1}{2}} = - \left(\left[1 + 4.4Re_b^{0.4} Pr \left(\frac{T}{T_{freezing}} \right)^{10} \left(\frac{k_p}{k_f} \right)^{0.03} \phi^{0.66} \right] + Rd\beta_w^3 \right) N'(0). \tag{28}$$

3. Mathematical Analysis

Highly nonlinear and coupled systems of differential equations usually possess no closed-form solution. Our flow model for $Al_2O_3 + H_2O$ is a highly nonlinear fourth-order model defined at a semi-infinite domain. Therefore, the model was tackled numerically using the Runge-Kutta scheme [13,16,25], as the RK scheme is used for the first order initial value problem (IVP). First the following substitutions were made and the model was reduced into first order IVP.

$$h_1 = L, \quad h_2 = L', \quad h_3 = L'', \quad h_4 = L''', \quad h_5 = N, \quad h_6 = N'. \tag{29}$$

After the successful transformation into the first order IVP, Mathematica 10.0 was used and the system was solved successfully.

4. Graphical Results and Discussion

This section emphasizes the flow and thermophysical characteristics of the fluid phase and the nanoparticles of Al_2O_3 . The values for the thermophysical characteristics were calculated at 310 K [23]. The results for the shear stress and heat transfer rate are elaborated using bar charts and are discussed comprehensively.

4.1. Velocity and Temperature Distribution

Magnetic field phenomena are of a great significance from an industrial point of view. Many industrial productions contain impurities that need to be removed. However, the magnetic parameter opposes the fluid motion, and the impurities remain at the bottom and the nanofluid velocity drops. The influence of Lorentz forces on the velocity distribution of $\text{Al}_2\text{O}_3 + \text{H}_2\text{O}$ nanofluids is elaborated in Figure 3a. It was shown that the applied magnetic field opposed the nanofluid motion, and the velocity of the $\text{Al}_2\text{O}_3 + \text{H}_2\text{O}$ nanofluid dropped. The velocity declined more slowly for a weaker magnetic field, and a rapid decrement in the nanofluid velocity was observed for a stronger magnetic field. Near the arched surface, variations in the velocity ($L'(\eta)$) were almost negligible. This behavior of the velocity distribution was due to the friction between the surface and the nanolayer of $\text{Al}_2\text{O}_3 + \text{H}_2\text{O}$. In the successive nanolayers, the velocity field was altered significantly. These influences became negligible far from the curve and showed an asymptotic pattern of velocity distribution at the free surface. Figure 3b shows the velocity distribution of the parameter m . The velocity of the $\text{Al}_2\text{O}_3 + \text{H}_2\text{O}$ nanofluid dropped rapidly for m in comparison with M . As the values for parameter m became larger, the velocity decreased promptly.

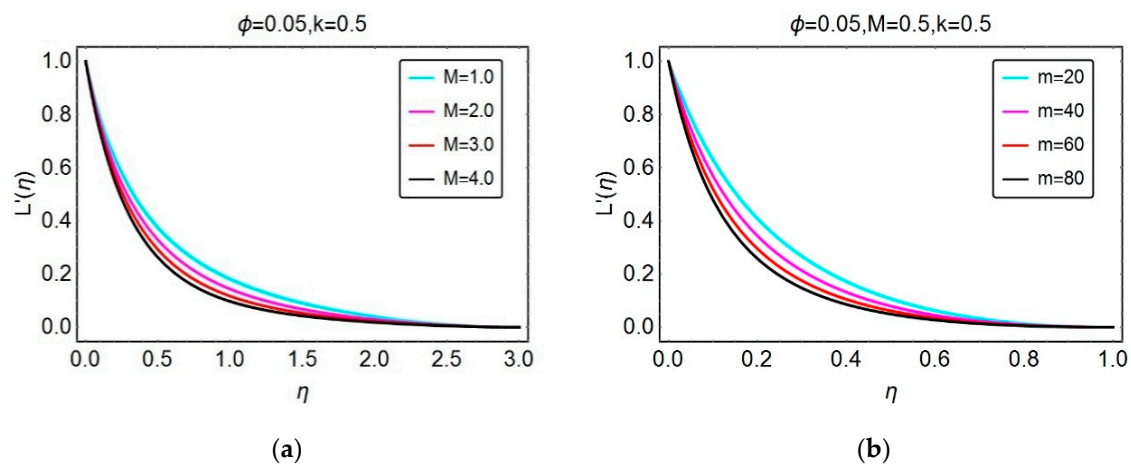


Figure 3. Impacts of (a) M and (b) m on the velocity distribution ($L'(\eta)$).

The effects of surface curvature on the velocity ($L'(\eta)$) are elucidated in Figure 4a. Altering the surface curvature caused the velocity to increase. For a smaller curvature, the velocity increased slowly and then vanished asymptotically far away from the surface. Similar behavior of the velocity of the $\text{Al}_2\text{O}_3 + \text{H}_2\text{O}$ nanofluid is depicted in Figure 4b. For α , a prominent behavior of the velocity was noticed in $0.5 \leq \eta \leq 1.5$. Besides this, the velocity ($L'(\eta)$) was almost inconsequential.

The temperature distribution ($N(\eta)$) for the radiation parameter (Rd) and Eckert number is highlighted in Figure 5a,b, respectively. In Figure 5a, we can see rapid drops in the temperature that were investigated by altering the radiation parameter (Rd). The temperature ($N(\eta)$) dropped rapidly for a stronger radiation parameter, however at the free surface this was almost negligible and vanished asymptotically. The Eckert number, which appeared due to viscous dissipation, played a vibrant role in the heat transfer enhancement. These effects are elucidated in Figure 5b. It was obvious that the temperature of $\text{Al}_2\text{O}_3 + \text{H}_2\text{O}$ nanofluid grew for the more dissipative nanofluid. For the larger Ec , the temperature distribution rose rapidly.

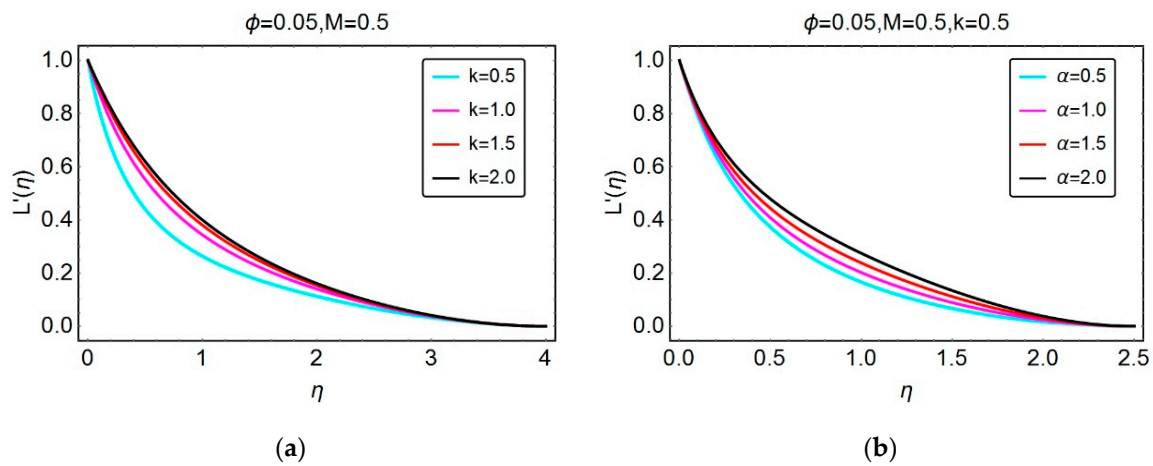


Figure 4. Impacts of (a) K and (b) α on the velocity distribution ($L'(\eta)$).

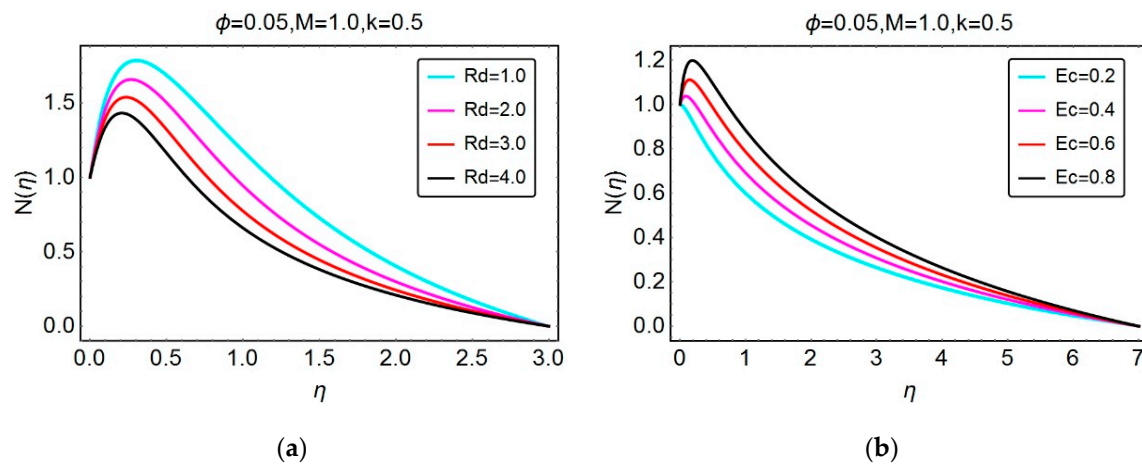


Figure 5. Impacts of (a) Rd and (b) Ec on the temperature distribution ($N(\eta)$).

4.2. Streamlines and Isotherms

This subsection is devoted to analyzing the behavior of the streamlines and isotherm patterns by altering different pertinent flow parameters. Figure 6 presents the streamline pattern by a varying magnetic parameter (M). For a smaller magnetic parameter, the streamlines were more curved near the surface and for a stronger M , the streamlines assumed a less curved shape. At the free stream, these streamlines became straight, since, as already mentioned for the parameter $m > 1$, it showed that it was a nonlinear stretching curved surface. The streamline pattern versus m is elaborated in Figure 7. It was noticed that by decreasing the parameter m , the streamlines assumed a more curved pattern. The curvature parameter showed a fascinating pattern for the streamlines, in comparison with M and m . These alterations are illustrated in Figure 8. Figure 9 depicts the flow pattern for varying α . For a higher α , the streamlines shrank and became almost straight at the top. Figure 10 elaborates the isotherm pattern for the radiation parameter (Rd). When there was more radiative nanofluid, the isotherms increased, and vice versa. Further, a 3D scenario of the isotherms is depicted in Figure 11.

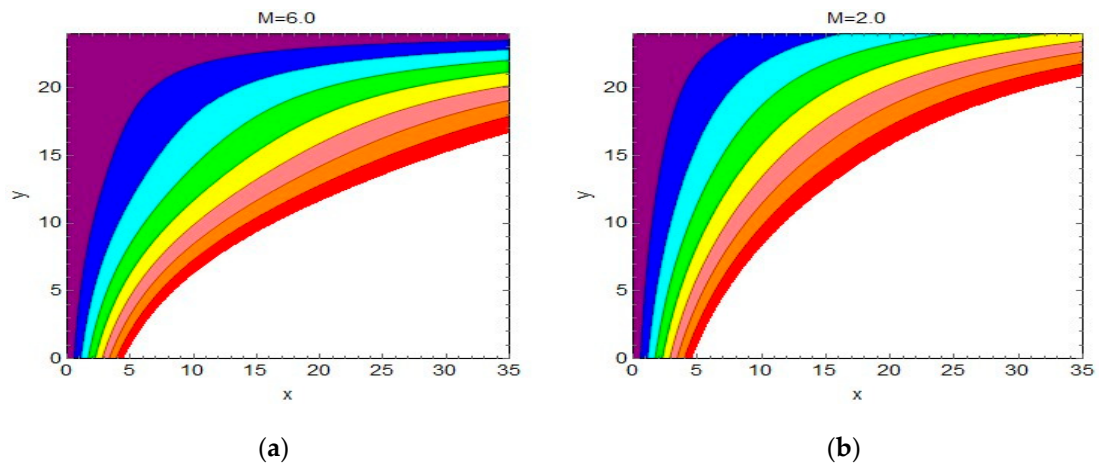


Figure 6. Streamlines for (a) $M = 6$ (b) $M = 2$.

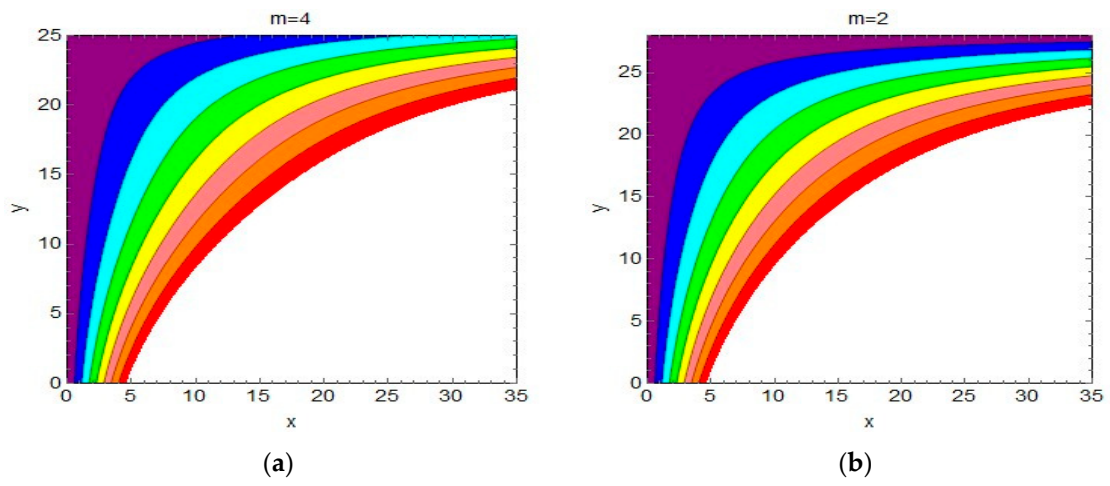


Figure 7. Streamlines for (a) $m = 4$ and (b) $m = 2$.

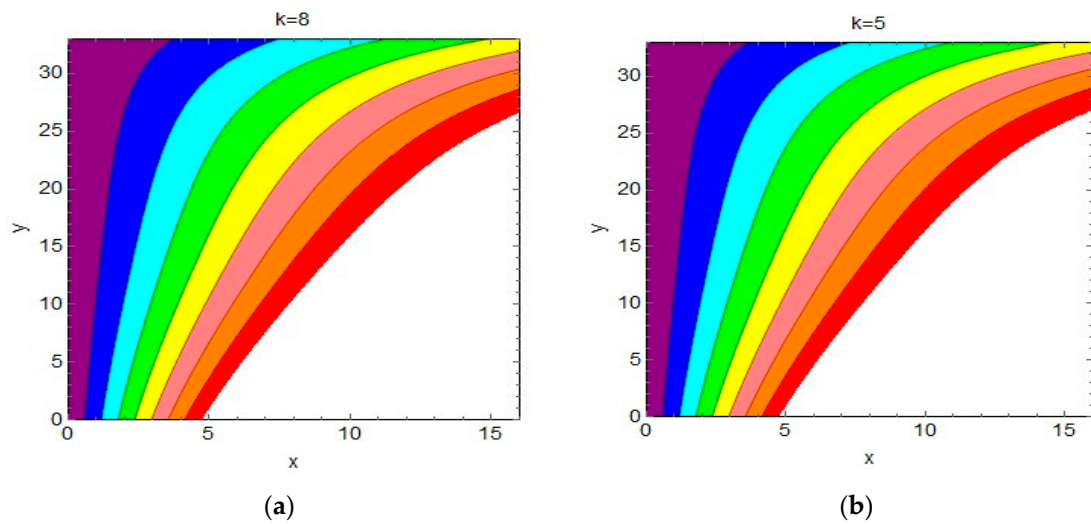


Figure 8. Streamlines for (a) $k = 8$ and (b) $k = 5$.

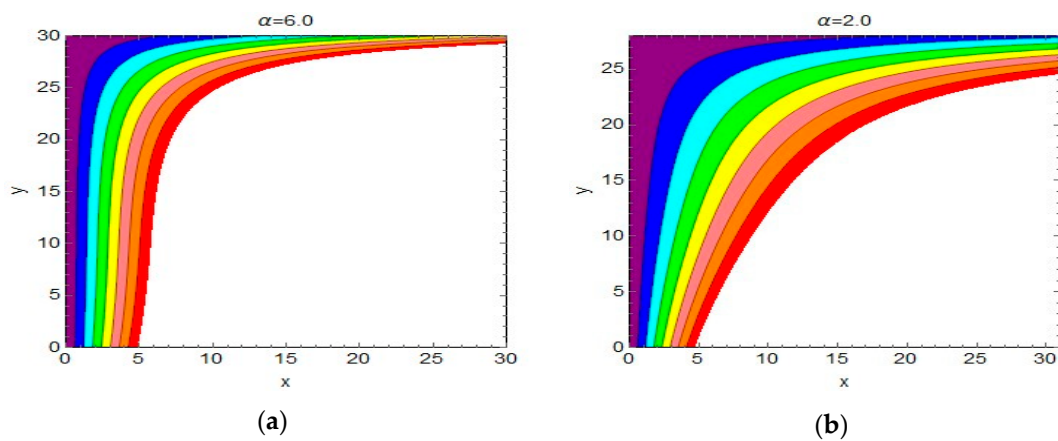


Figure 9. Streamlines for (a) $\alpha = 6$ and (b) $\alpha = 2$.

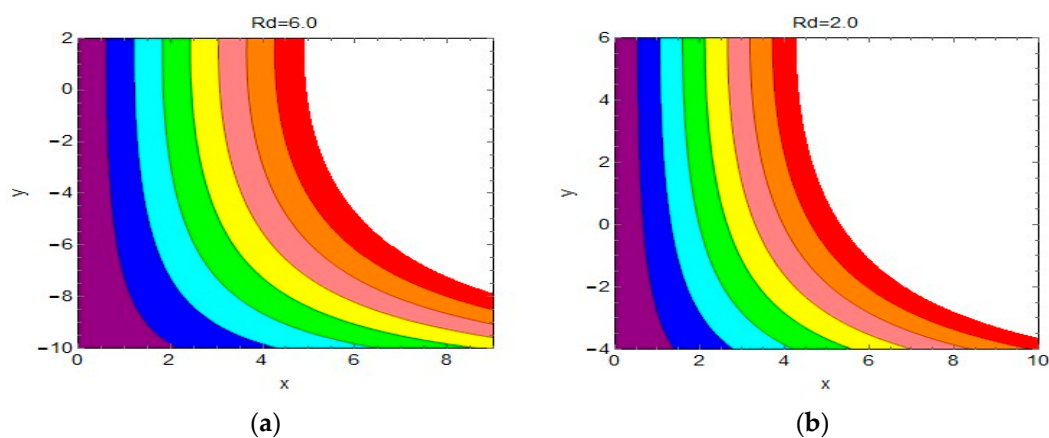


Figure 10. Isotherms for (a) $Rd = 6$ and (b) $Rd = 2$.

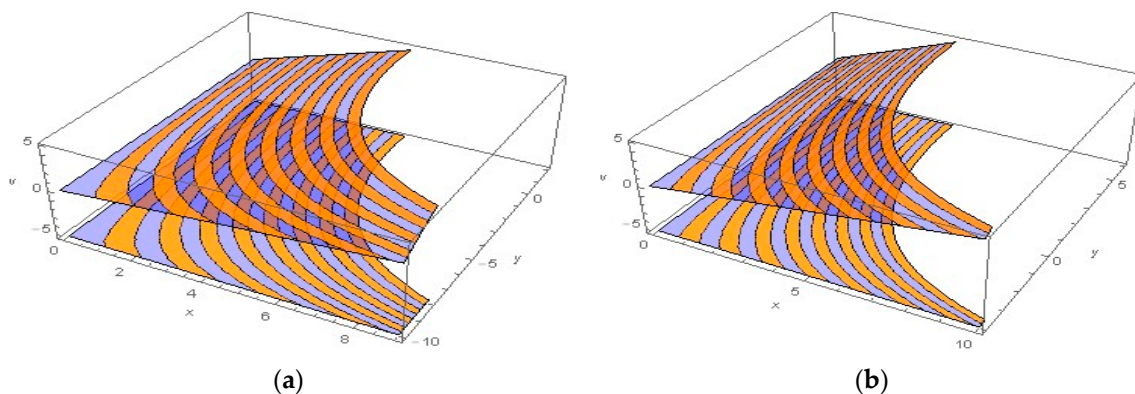


Figure 11. 3D scenario of Figure 10; (a) $Rd = 6$ and (b) $Rd = 2$.

4.3. Thermophysical Characteristics

This subsection describes the impacts of the volume fraction factor (ϕ) on the effective characteristics of the nanofluids, and the behavior of the shear stress and local heat transfer rate by varying embedded flow parameters.

Figure 12 describes the effects of the volume fraction (ϕ_v) and diameter of the nanoparticles on the effective dynamic viscosity of $\text{Al}_2\text{O}_3 + \text{H}_2\text{O}$. The volume fraction of Al_2O_3 showed a vibrant role in enhancing the dynamic viscosity of the nanofluid. The observed high dynamic viscosity corresponded to a greater volume fraction. On the other hand, the nanoparticle diameter (d_p) induced inverse variations in the dynamic viscosity. Increasing the diameter of the nanoparticles caused the dynamic

viscosity to drop. This means that nanoparticles with a smaller diameter are important to enhance the dynamic viscosity of nanofluids.

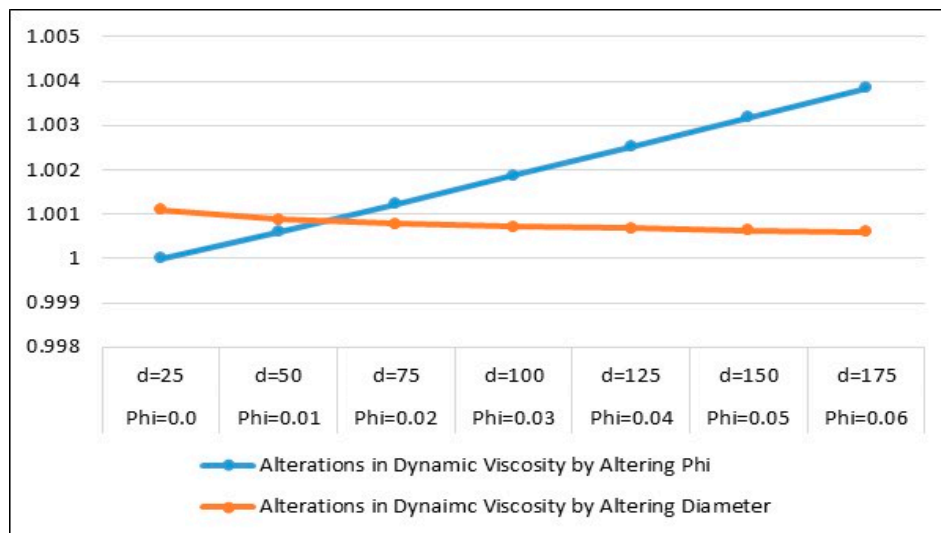


Figure 12. The impact of the volume fraction (ϕ) and the nanoparticle diameter (d_p) on the dynamic viscosity.

Figure 13 highlights the effective density (ρ_{nf}) and heat capacity ($(\rho c_p)_{nf}$) of the nanofluid versus ϕ . ϕ and ρ_{nf} were in direct proportion to each other, and the effective heat capacity dropped when ϕ increased. Therefore, smaller values of ϕ enhanced the effective heat capacity. Due to the high volume fraction, the colloidal suspension $\text{Al}_2\text{O}_3 + \text{H}_2\text{O}$ became denser, which enhanced the effective density (ρ_{nf}). Figure 14 highlights that the volume fraction (ϕ) and the effective electrical conductivity were in inverse proportion to each other.

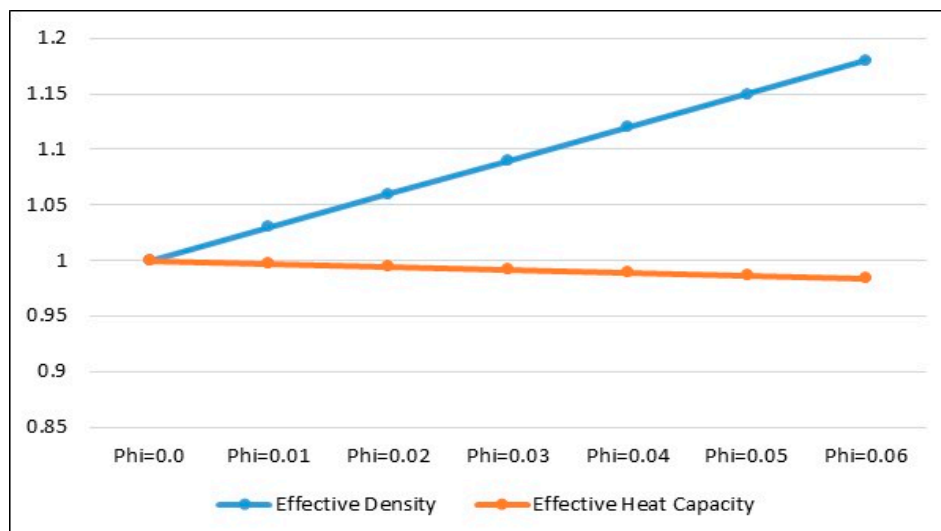


Figure 13. The impact of ϕ on the effective density and heat capacity.

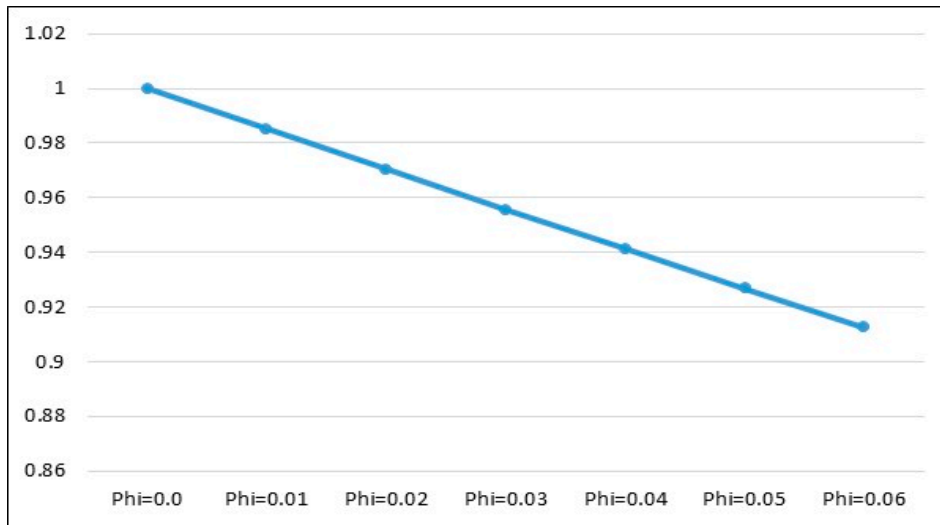


Figure 14. The impact of ϕ on the effective electrical conductivity.

4.4. Skin Fraction and Heat Transfer Rate

The shear stress and the local rate of heat transfer are very interesting and have attained great significance from an industrial point of view. The radiation parameter, Eckert number, and the curvature parameter all play a significant role in the shear stress and local Nusselt number. Figure 15 describes the heat transfer behavior for Rd , Ec , K and the volume fraction of the nanoparticles. It was noted that the more radiative nanofluids favored the heat transfer. On the other hand, a smaller amount of the heat transfer was noticed for a higher Eckert number. Therefore, the less dissipative fluids similarly favored the heat transfer. For a more curved surface, a large curvature worked against the heat transfer. At greater volume concentrations the heat transfer rate grew slowly.

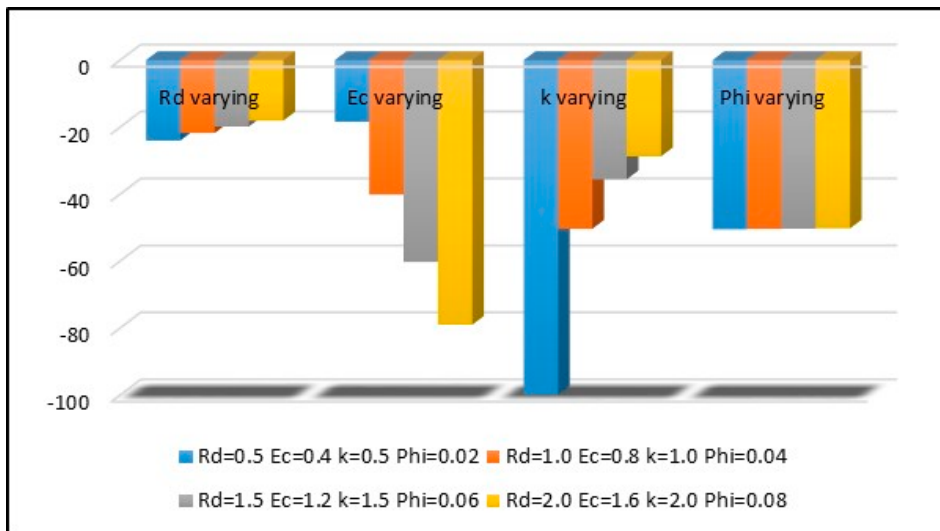


Figure 15. The impact of various flow parameters on the local heat transfer.

Figure 16 elucidates the shear stress behavior for the mixed convection parameter (α), magnetic parameter (M), curvature of the surface, and m . For a more convective fluid, the heat transfer increased rapidly at the surface. The magnetic parameter (M) highlighted the reverse behavior of the shear stress. With an increase of the parameter M , the shear stress dropped quickly, and an almost negligible influence of m on the shear stresses was also observed. Significant alterations were pointed out for surface curvature, as the curve was along the circle loop of radius a . Therefore, for a smaller radius,

shear stress declined promptly. Increasing the radius of the loop caused the surface curvature to become larger, which favored the shear stress.

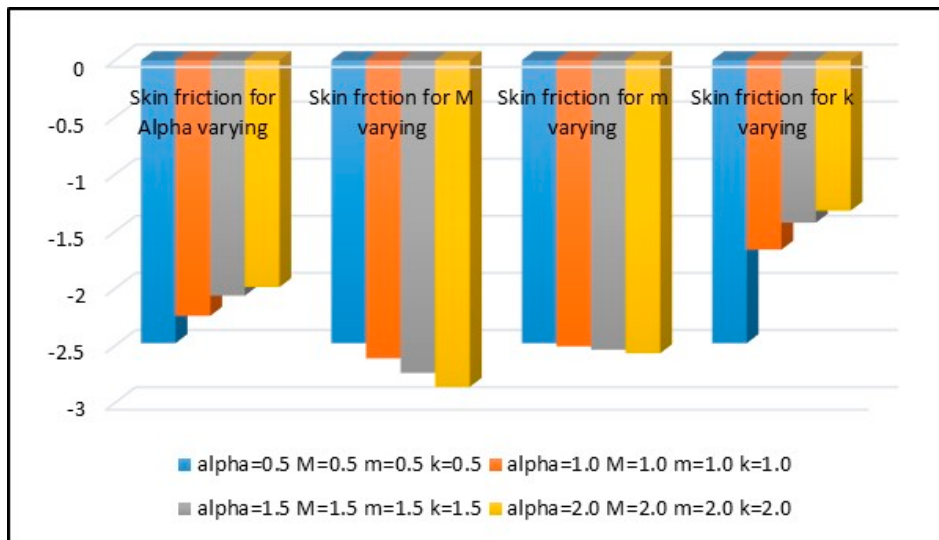


Figure 16. The impact of various parameters on the shear stress.

5. Conclusions

The mixed convective laminar flow of water, composed by Al_2O_3 nanofluids in the presence of Lorentz forces and nonlinear radiative heat flux, was examined over an arc-shaped geometry. To enhance the heat transfer rate, a thermal conductivity model that considered the impact of freezing temperature and molecular diameter was used. It was found that the nanofluid velocity ($L'(\eta)$) dropped for a stronger magnetic parameter (M), which is very significant from an industrial point of view. Further, the velocity of the nanofluid increased due to the mixed convection and larger curvature of the surface. The temperature $N(\eta)$ intensified for more dissipative fluid, and an inverse relationship between the temperature and the thermal radiation parameter was found. The dynamic viscosity of the nanofluid increased with the volume fraction, and the diameter of the nanoparticles showed reverse alterations for dynamic viscosity. The nanofluid became denser for a high volume fraction, and the electrical conductivity dropped. It was found that the heat transfer reduced the surface of a smaller curvature and intensified for larger curvatures. A more convective fluid and a larger curvature better opposed the shear stress. Finally, when considering the influence of the freezing temperature and the molecular diameter, the nanofluid flow model is very useful for heat transfer in comparison with existing studies.

Author Contributions: Conceptualization, U.K. and A.A.; methodology, Adnan, N.A.; software, S.N.; validation, writing—review and editing, I.K. and W.A.K.; supervision, S.T.M.-D; Funding acquisition, S.O.A. All the authors contributed to the manuscript equally.

Funding: This research received no external funding.

Conflicts of Interest: The authors declare no conflict of interest.

Nomenclature

u	Component of the velocity
a	Radius
T	Temperature
T_∞	Temperature far from the surface
k_f	Thermal conductivity of the host fluid
k_s	Thermal conductivity of the nanoparticles
k_{nf}	Effective thermal conductivity of the nanofluid
$(C_p)_f$	Heat capacity of the host fluid
σ_s	Electrical conductivity of the nanoparticles
σ_{nf}	Electrical conductivity of the nanofluid
μ_f	Dynamic viscosity of the fluid
M^*	Molecular weight
d_f	Molecular diameter
β_w	Temperature ratio parameter
Pr	Prandtl number
M	Hartmann number
$L(\eta)$	Dimensionless velocity
Nu	Nusselt number
v	Component of the velocity
p	Pressure
T_w	Temperature at the surface
ρ_f	Density of the host fluid
ρ_s	Density of the nanoparticles
ρ_{nf}	Effective density of the nanofluid
$(C_p)_s$	Heat capacity of the nanoparticles
$(C_p)_{nf}$	Heat capacity of the nanofluid
σ_f	Electrical conductivity of the host fluid
μ_{nf}	Effective dynamic viscosity
ϕ	Volume fraction of the nanoparticles
N^*	Avogadro number
k_b	Stefan Boltzmann constant
Rd	Radiation parameter
Ec	Eckert number
K	Curvature parameter
$N(\eta)$	Dimensionless temperature
C_f	Skin fraction coefficient

References

1. Choi, S. Enhancing thermal conductivity of fluids with nanoparticles in developments and applications of non-newtonians flows. *ASME J. Heat Transf.* **1995**, *66*, 99–105.
2. Clerk, M.J. *Treatise on Electricity and Magnetism*; Oxford University Press: Oxford, UK, 1873.
3. Bruggeman, D.A.G. Berechnung verschiedener physikalischer konstanten von heterogenen substanzen, I—dielektrizitatskonstanten und leitfähigkeiten der mischkörper aus isotropen substanzen. *Ann. Phys. Leipz.* **1935**, *24*, 636–679. [[CrossRef](#)]
4. Hamilton, H.L.; Crosser, O.K. Thermal conductivity of heterogeneous two-component systems. *Ind. Eng. Chem. Fundam.* **1962**, *1*, 187–191. [[CrossRef](#)]
5. Lu, S.; Lin, H. Effective conductivity of composites containing aligned spherical inclusions of finite conductivity. *J. Appl. Phys.* **1996**, *79*, 6761–6769. [[CrossRef](#)]
6. Koo, J.; Kleinstreuer, C. A new thermal conductivity model for nanofluids. *J. Nanopart. Res.* **2004**, *6*, 577–588. [[CrossRef](#)]

7. Koo, J.; Kleinstreuer, C. Laminar nanofluid flow in micro-heat sinks. *Int. J. Heat Mass Transf.* **2005**, *48*, 2652–2661. [[CrossRef](#)]
8. Xue, Q.Z. Model for thermal conductivity of carbon nanotube-based composites. *Phys. B Phys. Condens. Matter.* **2005**, *368*, 302–307. [[CrossRef](#)]
9. Prasher, R.; Bhattacharya, P.; Phelan, P.E. Thermal conductivity of nanoscale colloidal solutions (nanofluids). *Phys. Rev. Lett.* **2005**, *92*, 25901. [[CrossRef](#)]
10. Li, C.H.; Peterson, G.P. Experimental investigation of temperature and volume fraction variations on the effective thermal conductivity of nanoparticle suspensions (nanofluids). *J. Appl. Phys.* **2006**, *99*. [[CrossRef](#)]
11. Corcione, M. Rayleigh–Bernard convection heat transfer in nanoparticle suspensions. *Int. J. Heat Fluid Flow* **2011**, *32*, 65–77. [[CrossRef](#)]
12. Sheikholeslami, M.; Li, Z.; Shamlooei, M. Nanofluid MHD natural convection through a porous complex shaped cavity considering thermal radiation. *Phys. Lett. A* **2018**, *382*, 1615–1632. [[CrossRef](#)]
13. Ahmed, N.; Khan, A.U.; Mohyud-Din, S.T. Influence of an effective prandtl number model on squeezed flow of $\gamma\text{Al}_2\text{O}_3\text{-H}_2\text{O}$ and $\gamma\text{Al}_2\text{O}_3\text{-C}_2\text{H}_6\text{O}_2$ nanofluids. *J. Mol. Liq.* **2017**, *238*, 447–454. [[CrossRef](#)]
14. Sheikholeslami, M.; Zia, Q.M.Z.; Ellahi, R. Influence of induced magnetic field on free convection of nanofluid considering Koo-Kleinstreuer-Li (KKL) correlation. *Appl. Sci.* **2016**, *6*, 324. [[CrossRef](#)]
15. Asadullah, A.M.; Khan, U.; Naveed, A.; Mohyud-Din, S.T. Analytical and numerical investigation of thermal radiation effects on flow of viscous incompressible fluid with stretchable convergent/divergent channels. *J. Mol. Liq.* **2016**, *224*, 768–775.
16. Khan, U.; Naveed, A.A.; Mohyud-Din, S.T. 3D squeezed flow of $\gamma\text{Al}_2\text{O}_3\text{-H}_2\text{O}$ and $\gamma\text{Al}_2\text{O}_3\text{-C}_2\text{H}_6\text{O}_2$ nanofluids: A numerical study. *Int. J. Hydrog. Energy* **2017**, *42*, 24620–24633. [[CrossRef](#)]
17. Iijima, S. Helical microtubules of graphitic carbon. *Nature* **1991**, *354*, 56–58. [[CrossRef](#)]
18. Naveed, A.A.; Khan, U.; Mohyud-Din, S.T. Influence of thermal radiation and viscous dissipation on squeezed flow of water between two rigid plates saturated with carbon nanotubes. *Colloids Surf. A Physicochem. Eng. Asp.* **2017**, *522*, 389–398.
19. Saba, F.; Naveed, A.; Hussain, S.; Khan, U.; Mohyud-Din, S.T.; Darus, M. Thermal analysis of nanofluid flow over a curved stretching surface suspended by carbon nanotubes with internal heat generation. *Appl. Sci.* **2018**, *8*, 395. [[CrossRef](#)]
20. Khan, U.; Naveed, A.; Mohyud-Din, S.T. Heat transfer effects on carbon nanotubes suspended nanofluid flow in a channel with non-parallel walls under the effect of velocity slip boundary condition: A numerical study. *Neural Comput. Appl.* **2017**, *28*, 37–46. [[CrossRef](#)]
21. Reddy, J.V.R.; Sugunamma, V.; Sandeep, N. Dual solutions for nanofluid flow past a curved surface with nonlinear radiation, sores and dufour effects. *J. Phys. Conf. Ser.* **2018**, *1000*, 12152. [[CrossRef](#)]
22. Hayat, T.; Qayyum, S.; Imtiaz, M.; Alsaedi, A. Double stratification in flow by curved stretching sheet with thermal radiation and joule heating. *J. Therm. Sci. Eng. Appl.* **2017**, *10*. [[CrossRef](#)]
23. Alsabery, A.I.; Sheremet, M.A.; Chamkha, A.J.; Hashim, I. MHD convective heat transfer in a discretely heated square cavity with conductive inner block using two-phase nanofluid model. *Sci. Rep.* **2018**, *8*, 1–23. [[CrossRef](#)]
24. Corcione, M. Empirical correlating equations for predicting the effective thermal conductivity and dynamic viscosity of nanofluids. *Energy Convers. Manag.* **2011**, *52*, 789–793. [[CrossRef](#)]
25. Naveed, A.A.; Khan, U.; Mohyud-Din, S.T. Unsteady radiative flow of chemically reacting fluid over a convectively heated stretchable surface with cross-diffusion gradients. *Int. J. Therm. Sci.* **2017**, *121*, 182–191.

